Asymmetric polarization gating for spectral tuning and temporal confinement of high-order harmonics

C. Picot, J. Vábek, T. Němec, Stefan Skupin, E. Constant, F. Catoire

▶ **To cite this version:**

C. Picot, J. Vábek, T. Němec, Stefan Skupin, E. Constant, et al.. Asymmetric polarization gating for spectral tuning and temporal confinement of high-order harmonics. Physical Review A, 2025, 111 (2), pp.023110. 10.1103/PhysRevA.111.023110 . hal-04953390

HAL Id: hal-04953390
https://hal.science/hal-04953390v1

Submitted on 18 Feb 2025

HAL is a multi-disciplinary open access archive for the deposit and dissemination of scientific research documents, whether they are published or not. The documents may come from teaching and research institutions in France or abroad, or from public or private research centers.

L'archive ouverte pluridisciplinaire **HAL**, est destinée au dépôt et à la diffusion de documents scientifiques de niveau recherche, publiés ou non, émanant des établissements d'enseignement et de recherche français ou étrangers, des laboratoires publics ou privés.

Asymmetric polarization gating for spectral tuning and temporal confinement of high order harmonics

C. Picot,[1] J. Vábek,[2,3,4] T. Němec,[4] S. Skupin,[1] E. Constant,[1,*] and F. Catoire[2,†]

[1] *Institut Lumière Matière, UMR 5306 - CNRS, Université de Lyon 1, 69622 Villeurbanne, France*
[2] *Centre Lasers Intenses et Applications, Université de Bordeaux-CNRS-CEA, 33405 Talence Cedex, France*
[3] *ELI Beamlines Facility, The Extreme Light Infrastructure ERIC, Za Radnicí 835, 25241 Dolní Břežany, Czech Republic*
[4] *Czech Technical University in Prague – Faculty of Nuclear Sciences and Physical Engineering, Jugoslávských partyzánů 1580/3, 160 00 Praha 6, Czech Republic*

(Dated: February 18, 2025)

We analyze high order harmonic generation using the asymmetric polarization gating obtained by the combination of two delayed counter-rotating pulses with different peak amplitudes. It allows for a better understanding of polarization gated XUV generation in general, increases the control of the harmonic temporal confinement, and can be used for tuning the central frequency of the harmonic comb and optimizing the HHG efficiency. Experimental results clearly confirm the gate control and the XUV tunability, in agreement with a model based on the Strong Field Approximation.

I. INTRODUCTION

High order Harmonic Generation (HHG) has emerged as a prominent tabletop technique for generating ultrashort XUV beams [1]. This method offers unique properties such as spatial and temporal coherence of the XUV beam [2, 3], precise control of the harmonics polarization state [4], and the generation of ultra-short XUV pulses [5, 6], making HHG invaluable for attosecond science [7–10]. Its application in spectroscopy and time-resolved studies is well established in both gas phase [11] and condensed phase [12] scenarios. The HHG spectrum consists of odd harmonics of the frequency of the fundamental driving pulse, reflecting the spherical symmetry of atomic systems, as well as the periodicity and coherence of attosecond bursts. XUV spectroscopy involves selecting specific harmonics from this spectrum [13–15]. Most characteristics of the produced XUV radiation, such as amplitude and polarization state, are increasingly well controlled and tunable, even if precise tuning of the central XUV frequency and attosecond chirp remains a challenge.

Producing isolated attosecond pulses is a significant achievement in the HHG research field, facilitated by techniques such as intensity gating, polarization gating, time-dependent phase matching, etc. Polarization gating [16–25] – the focus of this article – exploits the sensitivity of the HHG process to the ellipticity of the driving field. Modulating the field ellipticity in time by superimposing two counter-rotating circularly polarized delayed pulses makes it possible to confine the XUV emission inside a polarization gate and generate ultrashort pulses. At the center of the temporal gate, the two pulses overlap with equal amplitude, and the pump polarization briefly becomes nearly linear. Because HHG is most efficient for linear polarized driving fields, an effective confinement of XUV emission within the polarization gate occurs, thus also enabling the generation of isolated attosecond pulses when sub-half-cycle gates are created.

The harmonic yield as a function of the ellipticity ϵ of the driving field can be described by a Gaussian function, $\exp\left[-(\epsilon/\epsilon_q^{\mathrm{th}})^2\right]$ [26, 27], where ϵ_q^{th} is a parameter that is typically of the order of 0.13 for a 800 nm driving wavelength and is dependent on the harmonic order q. Thus, the harmonic yield is very sensitive to the ellipticity of the input field. This can be explained physically by the fact that in an elliptical field the ionized electron does not return to its parent ion during the recollision process but is displaced laterally, which leads to a less efficient recombination mechanism. The nature of the dependence of the harmonic yield on the ellipticity of the driving field as described above is specific to gazeous atomic and molecular systems and differs quite drastically in solids [28, 29]. In the standard polarization gate configuration, the amplitudes of the two counter-rotating fields are equal, and therefore the gate is always located at the center of the pulse. The scenario involving two different amplitudes – here referred to as Asymmetric Polarization Gating (APG) [24, 30] – offers greater control over the high harmonics, in particular their cut-off, and leads to further interesting properties of the generated XUV field [24, 25, 30–33]. Specifically, in this article we demonstrate experimentally and theoretically that it is possible to control the temporal position of the gate within the pulse without changing the gate duration. We also provide a thorough examination of the consequences of APG on the physics of HHG and, in particular, highlight the contributions of long and short trajectories. Finally, we demonstrate the ability to control the entire high harmonic spectrum and, in particular, the tunability of the harmonic central frequency.

* eric.constant@univ-lyon1.fr
† fabrice.catoire@u-bordeaux.fr

II. ASYMMETRIC POLARIZATION GATING

The standard Polarization Gating (PG) technique involves the combination of two delayed counter-rotating circularly polarized pulses (see Fig. 1). By using fields of different amplitudes, we achieve the Asymmetric Polarization Gating (APG), where the harmonic emission is confined in a gate that can be positioned arbitrarily within the driving pulse envelope. Sec. II A details the operational principles of APG in various regimes by means of a simple analytical expression for the harmonic dipole response. In particular, we investigate the scenario where the intensity envelope of the pump pulse changes approximately linearly across the gate and discuss how this can shift the harmonic comb in frequency. In Sec. II B, we present theoretical results based on the Strong Field Approximation (SFA) and compare them with anticipated outcomes from the simple dipole approach described in Sec. II A.

A. Principle

Following Ref. [34], for a linearly polarized driving field, the dipole response of a given harmonic q associated with HHG for a given quantum trajectory can be approximated by

$$d(t) = I^{\frac{q_{\text{eff}}}{2}}(t)\, e^{-i\varphi_q(t)} \approx e^{-iq\omega_0 t} I^{\frac{q_{\text{eff}}}{2}}(t)\, e^{-i\alpha_q I(t)}\,. \quad (1)$$

Here, $\varphi_q(t)$ is the phase associated with the dipole of harmonic q, ω_0 is the central frequency of the driving IR field, and q_{eff} and α_q are positive quantities that characterize harmonic yield and phase, respectively. $I(t)$ is the intensity envelope of the IR driving field – defined as the cycle averaged Poynting flux in propagation direction. In Eq. (1), we have used the linear approximation of the phase dependence φ_q with intensity: $\varphi_q(t) \approx \alpha_q I(t)$ where we thus assume that α_q is a given parameter for each harmonic. When superimposing two counter-rotating circularly polarized fields, the intensity envelope of the total field follows a more complex distribution and depends on the delay, dephasing, and amplitude ratio. In short, the linearly polarized portion of the total field (gate) is located where the two counter-rotating fields have the same amplitude. The position of the gate is therefore defined by the ratio of the two field amplitudes and their relative delay. To illustrate the impact of the relative delay on APG, different configurations of field amplitudes and delay are shown in Fig. 1.

In APG, the position of the gate within the driving pulse can thus be shifted by adjusting the amplitude ratio of the two pulses. According to the dipole model Eq. (1), the instantaneous frequency of a given harmonic q is provided by

$$\frac{d\varphi_q(t)}{dt} = \omega_q(t) \approx q\omega_0 + \alpha_q \frac{dI}{dt}\,. \quad (2)$$

This expression is obtained as the first order Taylor expansion of the phase φ_q with respect to the intensity. With linearly polarized drivers (i.e. without polarization gating), it gives rise to the well known frequency broadening of a given harmonic [34, 35] due to its generation over the full duration of the pulse. In contrast, when the XUV emission is confined inside the polarization gate, only the characteristics of the IR pulse in the gate are relevant for the emitted XUV light. In the situation where the intensity envelope of the IR driving field in the gate evolves with a linear slope characterized by ω_s [see Fig. 1(c)], $I(t) \approx I_0(1+\omega_s t)$, the effective frequency Eq. (2) can be written as $\omega_q = q\omega_0 + \alpha_q I_0 \omega_s$. Thus, the frequency shifts of the harmonics can be controlled by the slope ω_s.

Considering the case of plateau harmonics for which the coefficient $\alpha_q \approx \alpha$ is almost the same for all harmonics, the entire frequency comb is shifted by $\Delta\omega = \alpha I_0 \omega_s$. Information about the shape of the driving pulse and the position of the gate is thus encoded in the frequency content of the harmonic comb. In particular, locating the gate in the rising or falling front of the pulse allows one to shift the central harmonic frequency to the blue or red, respectively, as the slope parameter ω_s has the opposite sign. By contrast, in the plateau and in the transition from the plateau to the cut-off, α_q changes significantly with harmonic order, and thus $\Delta\omega_q = \Delta\alpha_q I_0 \omega_s$ will change from one harmonic to the next. This could provide a way to control the harmonic chirp in this frequency range. In the next section, we will demonstrate, in the framework of the SFA model, the effectiveness of this control of the frequency comb by APG.

B. Comparison to the SFA model

We start by describing our theoretical model based on the Strong Field Approximation (SFA) [36]. The model consists in writing the wave function as the sum of the ground state wave function – assumed unaffected – and a wave packet in the continuum. Neglecting the continuum-continuum transitions, one can express the dipole moment associated with the HHG in atomic units (a.u.) as

$$\mathbf{d}(t) = 2Re\Big\{ i \int_0^t d\tau \int d\mathbf{k} \mathbf{T}^*[\mathbf{k} - \mathbf{A}(t)] \times e^{-iS(\mathbf{k},t,\tau)} \mathbf{E}(\tau).\mathbf{T}[\mathbf{k} - \mathbf{A}(\tau)] \Big\}. \quad (3)$$

In this expression, $\mathbf{A}(t)$ is the vector potential defining the pump electric field $\mathbf{E}(t) = -\frac{\partial \mathbf{A}(t)}{\partial t}$ in the dipole approximation. $\mathbf{T}(\mathbf{k}) = \langle \mathbf{k}|\, \mathbf{r}\, |\varphi_0\rangle$ is the matrix amplitude transition from the ground state $|\varphi_0\rangle$ to the continuum state $|\mathbf{k}\rangle$ described by a plane wave. We note that the ground state is assumed to be an s orbital. Finally, the classical action is provided by $S(\mathbf{k}, t, \tau) = \frac{1}{2}\int_\tau^t dt' [\mathbf{k} - \mathbf{A}(t')]^2 + (t-\tau) I_p$. From the Eq. (3), one can recognize the contribution of the three main steps leading to

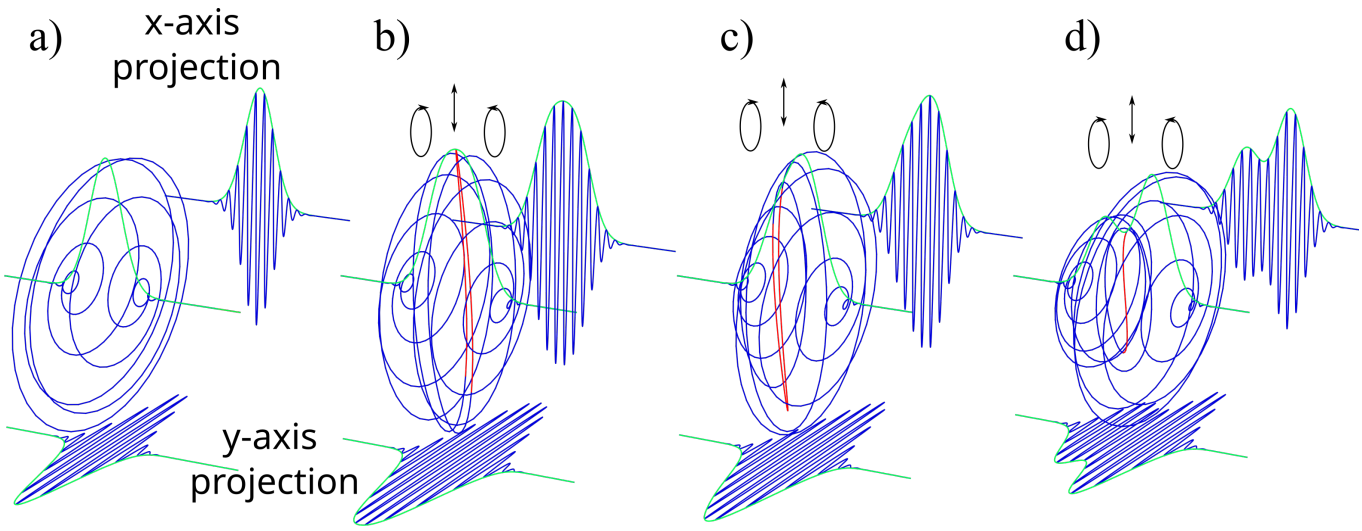

FIG. 1: Schematic of the principle of polarization gating for different configurations. Case a) corresponds to a single circularly polarized pulse that does not produce a polarization gate. The electric field amplitude is plotted in blue, and the intensity envelope of the pulse is represented by a green curve. In case b), the amplitudes of the two delayed counter-rotating pulses are equal, and the delay is taken as the pulse duration. The section of the electric field amplitude marked in red corresponds to an ellipticity below 0.1, i.e. the polarization is almost linear. In this situation, the intensity envelope is almost constant across the gate. In case (c), the two pulses have different amplitudes, while the delay is again taken as the pulse duration. In contrast to case (b), the intensity envelope has a significant linear slope across the gate. In case d), the amplitudes of the two pulses are different and the delay is larger than the pulse duration (1.7 times the pulse duration). The intensity envelope exhibits a minimum at the gate position.The back and bottom panels are the projection of the field evolution on the initial polarization x-axis and its perpendicular direction describing the polarization plane.

HHG, namely : i- Ionization $\mathbf{E}(\tau).\mathbf{T}[\mathbf{k}-\mathbf{A}(\tau)]$, ii- Propagation $e^{-iS(\mathbf{k},t,\tau)}$ and iii- Recombination $\mathbf{T}^*[\mathbf{k}-\mathbf{A}(t)]$. The manifold integral can be computed numerically, but here we use the saddle point method for the momentum integration. This leads to the following equation $\nabla_{\mathbf{k}} S(\mathbf{k},t,\tau)|_{\mathbf{k}=\mathbf{k}_S} = \mathbf{0}$, the solution of which is provided by

$$\mathbf{k_S} = -\frac{\int_\tau^t dt' \mathbf{A}(t')}{t-\tau}. \tag{4}$$

Using this momentum solution of the saddle point equation is equivalent to conservation of momentum between the ionization step and the recombination step. The momentum integration is then contracted using

$$\int d\mathbf{k} \to J(t-\tau) = \lim_{\eta\to 0^+} \left[\frac{\pi}{\eta + i(t-\tau)/2}\right]^{\frac{3}{2}}, \tag{5}$$

and the dipole can be finally computed as

$$\mathbf{d}(t) = 2Re\Big\{ i\int_0^t d\tau J(t-\tau)\mathbf{T}^*[\mathbf{k_S}-\mathbf{A}(t)] \times e^{-iS(\mathbf{k_S},t,\tau)}\mathbf{E}(\tau).\mathbf{T}[\mathbf{k_S}-\mathbf{A}(\tau)]\Big\}. \tag{6}$$

This formulation preserves the quantum nature of the process: it contains the interference of different quantum trajectories and does not pose any complications at the cut-off (compared to the time-resolved saddle points [36]), where different quantum trajectories merge leading to a cusp-like phenomenon [37]. In addition, it shows very good quantitative agreement with the rigorous numerical integration [38]. Finally, the harmonic spectrum is provided by the Fourier transform of the time-dependent dipole given in Eq. (6).

To evaluate APG with our SFA model, we describe the total field as the sum of the two counter-rotating fields delayed by the time t_d,

$$\mathbf{E}(t) = \mathbf{E}_{\circlearrowleft}(t) + \mathbf{E}_{\circlearrowright}(t-t_d)\,. \tag{7}$$

The field $\mathbf{E}_\epsilon(t)$ is written as

$$\mathbf{E}_\epsilon(t) = \frac{E_0}{\sqrt{1+\epsilon^2}} E_v(t)\left[\cos(\omega_0 t)\mathbf{e}_x + \epsilon\sin(\omega_0 t)\mathbf{e}_y\right]. \tag{8}$$

The field vector defines a polarization plane perpendicular to the propagation axis ($\mathbf{e}_z$). ω_0 is the central frequency and E_0 the amplitude of the envelope defined by $E_v(t)$. In our simulations, we used a $\cos^2$ envelope. The parameter ϵ sets the ellipticity of the field, and $\epsilon = -1$ corresponds to the left-handed circularly polarized field $\mathbf{E}_{\circlearrowleft}$ and $\epsilon = 1$ corresponds to the right-handed circularly polarized field $\mathbf{E}_{\circlearrowright}$. Using such a complex field, the question of the contribution of the initial state can raise. For example, considering a p orbital, one has to account for

the contribution of all the m quantum numbers of the initial state. This question is beyond the scope of this article and is left for future work. As already stated, in this article we will only consider an initial s orbital.

In order to confirm the frequency tuning of the harmonic spectrum induced by the APG, we have performed SFA calculations of the harmonic spectra using a pulse with the following characteristics: FWHM of 551 a.u. (13 fs) for both pulses, a delay of $t_d = 660$ a.u. (15.8 fs), a field amplitude at time $t = 0$ of $E_0 = 0.057$ a.u. (which corresponds to a peak intensity of 2.1×10^{14} W/cm^2). In order to create the aforementioned intensity slope inside the gate, one of the two pulses - whether the first or second determines the sign of the slope - has an amplitude that is larger by a factor 1.71. Figure 2 shows two illustrative APG configurations. In case (a), the first pulse has the lower amplitude, giving rise to a positive slope of the envelope inside the gate. In case (b), the amplitude ratio of the two pulses is inverted and the gate is shifted to the falling front of the pulse, resulting in a negative slope of the envelope.

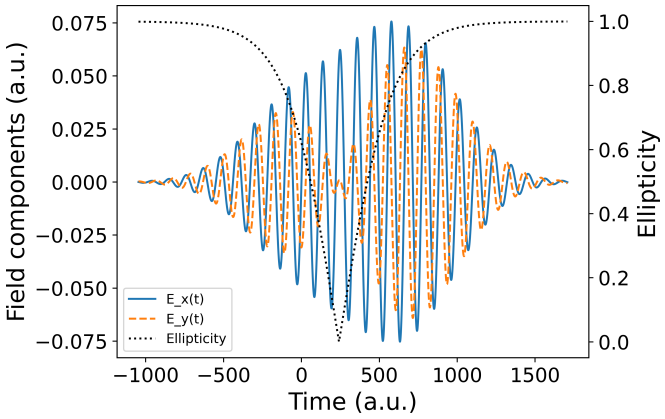

(a) APG with positive slope

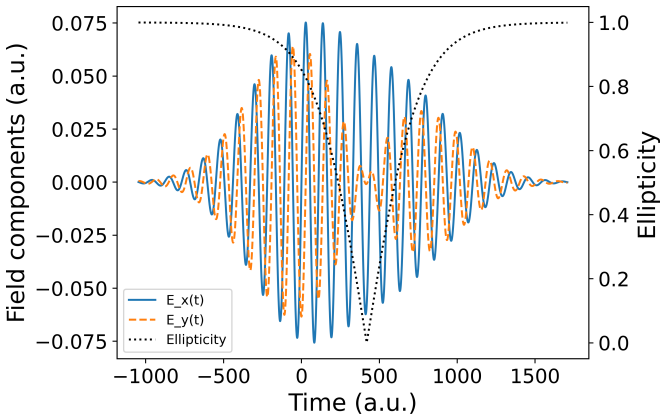

(b) APG with negative slope

FIG. 2: Schematic of the temporal evolution of the electric field projected on the x an y axis. The polarization gate is located at the position where $E_y = 0$ and can be moved through the pulse envelope in the rising front (a) or in the falling front (b) of the pulse.

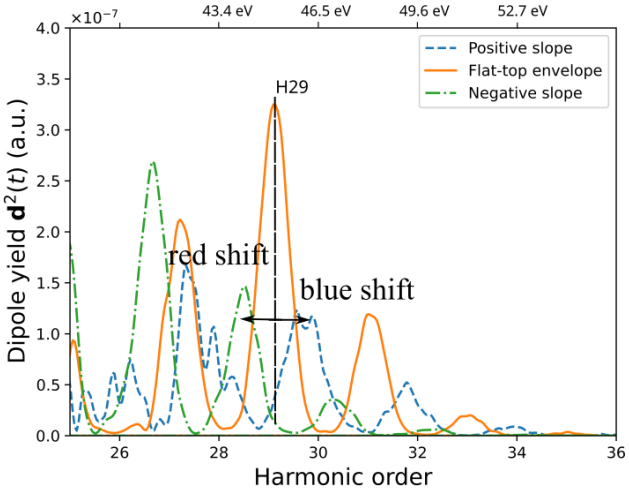

FIG. 3: Cut-off harmonic spectrum obtained from the SFA model for the APG fields plotted in Fig. 2. The dashed blue and dashed green curves are the harmonic spectra for the positive and negative intensity slopes in the gate, respectively. The orange curve is the reference spectrum associated with the standard PG configuration where the gate is located at the center of the pulse. We can observe the corresponding frequency shift of H29 as described in the text.

The corresponding cut-off harmonic spectra obtained from our SFA model are shown in Fig. 3. We focus on harmonics belonging to the cut-off region where both short and long trajectories merge descibed by a single value $\alpha_{\text{cut-off}}$. The reference spectrum (i.e. using two pulses with equal amplitudes resulting in a flat-top envelope in the gate) is plotted in full orange. The spectrum corresponding to the positive slope [Fig. 2(a)] is plotted in dashed blue and is clearly blue shifted (shifted toward the larger frequencies). In contrast, the spectrum for the negative slope [Fig. 2(b)] plotted in dashed green is red-shifted. If we now look carefully at the amplitude of the frequency shift, we can see that both spectra are shifted by roughly one harmonic order, that is, the red-shifted peak of H29 overlaps with the blue-shifted peak of H27. In the cut-off region the picture of frequency shift is rather clear since only one class of trajectory is involved leading to well-defined harmonics. In the following, we will compare the theoretical results presented here with the experimental results and extend the analysis to the whole spectral range of HHG. We will investigate to what extent our findings hold in the plateau region, where the situation is more complex due to the coherent contribution of both short and long trajectories [27], cf. Sec. IV. This increased spectral complexity already appears from the behavior of the harmonic H27 in Fig. 3, which has multiple peaks, consistent with the short duration of the high-harmonic pulse trains emitted [39]. Moreover, to perform this analysis, we will consider in the following more realistic driver fields.

III. EXPERIMENTAL RESULTS

We performed experiments to study the predicted frequency shift of the harmonics in APG. The experimental setup consists of a Ti:Sapphire laser system delivering 30 fs pulses at 800 nm with a repetition rate of 5 kHz. The beam is spatially filtered by propagation in an empty hollow core capillary. After propagation in the capillary, the pulse duration is fine-tuned by a set of chirped mirrors and a pair of fused silica wedges to obtain the shortest pulse duration. We obtain pulses with duration of 28 fs for high harmonic generation. Polarization control is performed by transmitting the pulse through two quartz waveplates [19, 25]. The first waveplate is a multi-order (MO) quartz waveplate, with a measured thickness of 841 μm, inducing a delay of $t_d = 27.3$ fs between two pulses polarized along the slow and fast axes. The second waveplate is an achromatic zero-order (ZO) $\lambda/4$ waveplate. The schematic of the polarization control setup is shown in Fig. 4.

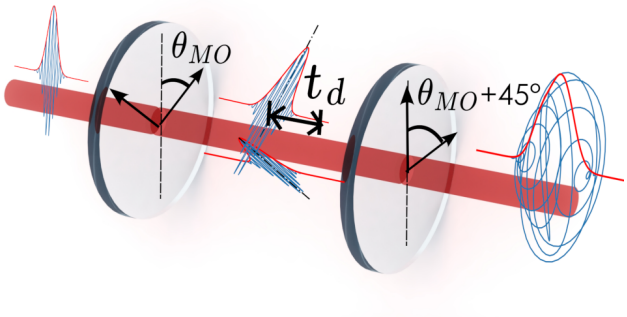

FIG. 4: Schematic of the polarization control setup composed of two quartz plates with their optical axes oriented at 45 deg to each other. This relative angle between the two plates is kept constant. The angle θ denotes the angle between the orientation of the input linearly polarized field kept on the vertical axis and the optical axis of the first waveplate.

The two waveplates are used at normal incidence. There is a 45 deg ($\pm$1 deg angle between the optical axes of the two plates to obtain the minimum width of the gate. The position of the gate in the pulse is controlled by rotating both plates while keeping constant their relative angle. A 1-mm thick birefringent calcite plate is inserted upstream, with, e.g., its fast axis oriented along the input laser polarization. This plate used at normal incidence introduces a roughly 500 fs delay between the components polarized along the slow and fast axes. Thus, after passing through the calcite plate, the linearly polarized main pulse and any potential noise polarized at 90 deg are temporally separated. This "temporal polarizer" guarantees that the pulse entering the polarization control setup is perfectly linearly polarized over its entire

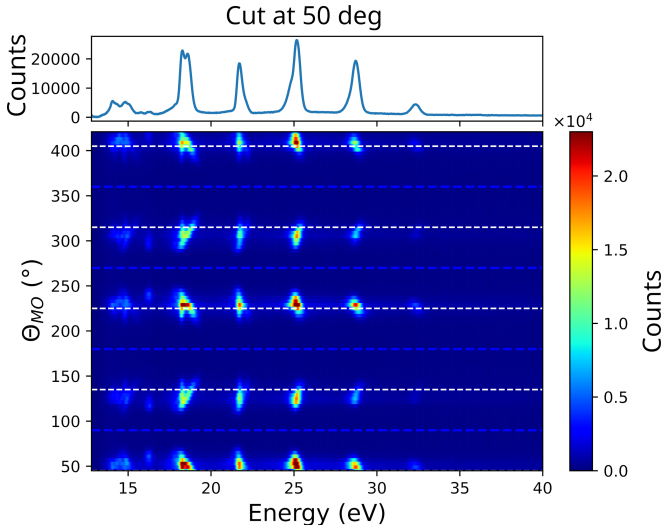

FIG. 5: Evolution of the experimental harmonic spectra as a function of the orientation of the polarization setup (angle θ_{MO}). The input pulse has a duration of 28 fs at 800 nm and a peak intensity of 2×10^{14} W/cm^2.

duration. The IR beam is then reflected at quasi-normal incidence by two silver-coated mirrors: a flat folding mirror and a focusing mirror with 60 cm focal length located 20 cm away from the 1 mm thin SiO_2 window of the vacuum chamber where HHG occurs. The beam waist is 50 μm in the generating medium. Harmonics are generated inside a 6 mm gas cell filled with Ar and analyzed with a flat field spectrometer that has a 150 μm wide input slit. The spectrometer is equipped with a 300 gr/mm grating, which yields a resolution of 100 to 200 meV throughout the observed XUV spectrum. The harmonic spectrum plotted as a function of the orientation of the first waveplate θ_{MO} is presented in Fig. 5.

We observe that the harmonic emission remains efficient in a large range of θ_{MO} (approximately 20 deg for plateau harmonics). Moreover, it follows a periodicity of 180 deg and a 90 deg mirror symmetry, as expected. We also observe that the central frequencies of the cut-off harmonics change regularly with θ_{MO}. This is also the case for plateau harmonics that split in two peaks with a variable relative spectral shift. The signal is not maximum at the "centered gate" position indicated by the white dashed lines in Fig. 5. This shift is about 4 deg, and the signal is maximum when the gate is in the falling front. This discrepancy with the theoretical results can be attributed to collective effects or the ionization process since in the SFA simulations, the population of the ground state is not included.

To better visualize the evolution of the spectrum with respect to θ_{MO}, Fig. 6 shows the data of Fig. 5, normalized to its maximum value for each value of θ_{MO}. For the plateau harmonics, we observe two peaks that behave differently with θ_{MO}. One is barely shifted with θ_{MO},

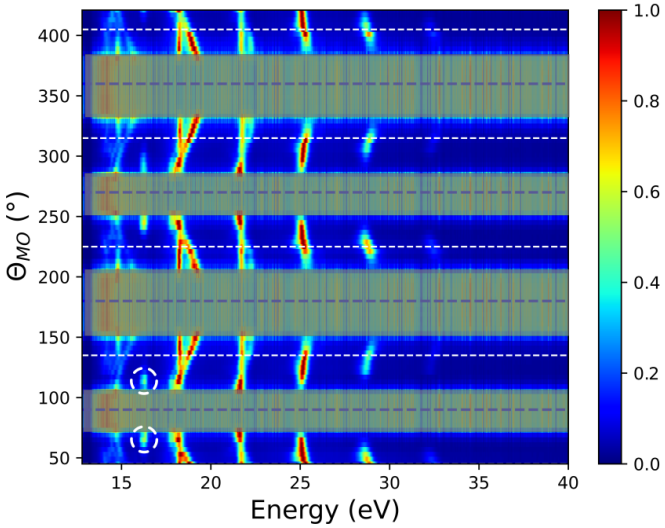

FIG. 6: Same as Fig. 5, but normalized to the maximum signal for each angle Θ_{MO}. In the grey areas the harmonic signal is too small to give meaningful results. The dashed white circles indicate the XUV emission associated to the Rydberg states as discussed at the end of Sec. IV.

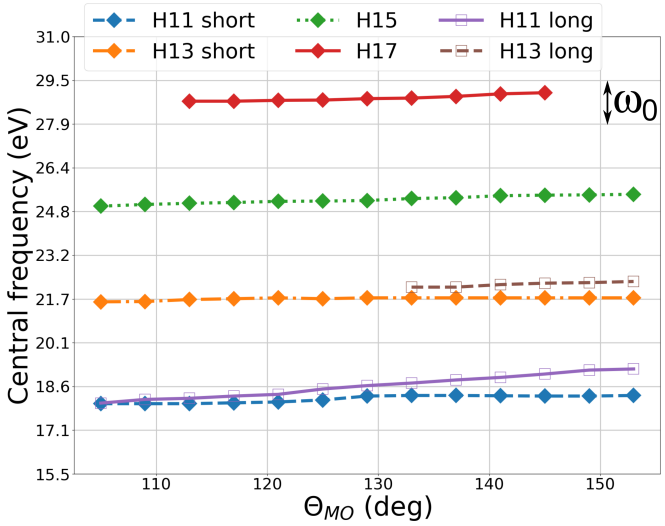

FIG. 7: Plot of the central frequency evolution value – for H11 to H17 – as a function of θ_{MO}. The short and the long trajectories are presented when they are separated. The grid on the y-axis has a spacing equal to the photon energy as indicated in the figure.

while the other is strongly shifted. This experimentally observed behavior is in accordance with the theoretical predictions from both the simple dipole model and the SFA presented in the previous section. The experimental data are further analyzed and compared with theory in the next section, in particular, to trajectory-dependent behavior. The experimental values of the energy shift for the different harmonics are summarized in Fig. 7. We observe that the frequency shift is the strongest for the long path plateau harmonics and lowest for short path plateau harmonics. The shift observed for cut-off harmonics is in between both.

IV. DISCUSSIONS

In this section, we discuss the experimental results in the light of numerical simulations based on the SFA model introduced in Sec. II B. All values of α are given in units of 10^{-14} cm^2/W. In order to compare the theory with the experimental results, the SFA model has to be evaluated for a pump driving field close to the experimental realization. To do so, the electric field is represented as a two-vector component $\mathbf{E} = (E_x, E_y)$. We then use matrices associated with the different optical elements, namely $\mathbb{O}_{MO}$ and $\mathbb{O}_{ZO}$ for the multi-order waveplate and the 0^{th} order waveplate, respectively. The input field is set to $\mathbf{E}_{in} = (E(t), 0)$, and the resulting field is $\mathbf{E}_{out} = \mathbb{O}_{ZO}\mathbb{O}_{MO}\mathbf{E}_{in}$. The explicit forms of the matrices and in particular their dependence on the angle θ_{MO} are provided in Appendix . A. The resulting

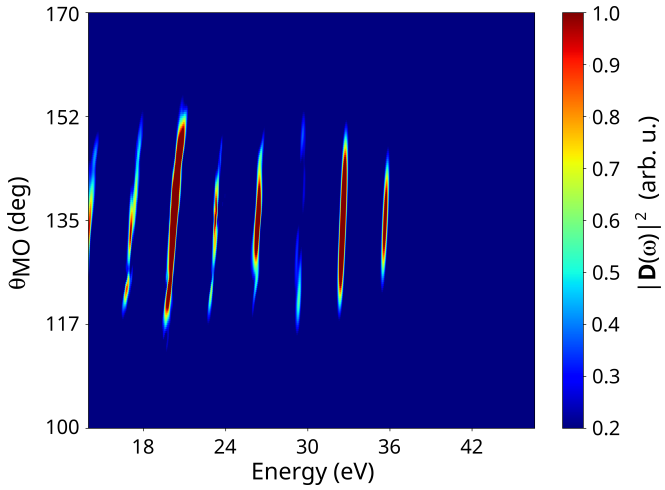

FIG. 8: Theoretical result of the SFA model for an input pulse duration of 20 fs at 800 nm. A peak intensity of the input field of 2×10^{14} W/cm^2 is assumed, and the SFA model is evaluated for polarization gating with a polarization control setup as used in the experiment, see text and App. A for details. The Harmonic yield distribution is thus plotted as a function of θ_{MO}.

field can be written in the form of Eq. (7), where relative amplitude and phase have a rather complex dependence on θ_{MO}. The theoretical spectra calculated with the SFA model for this field as a function of θ_{MO} are

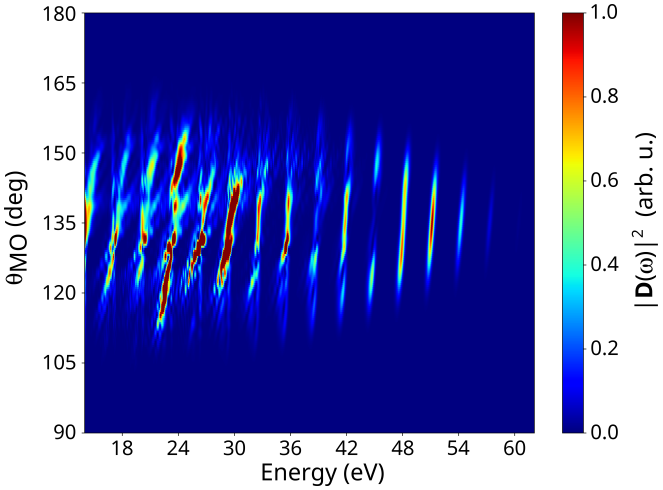

FIG. 9: Same as Fig. 8, but with twice the input intensity of 4×10^{14} W/cm^2.

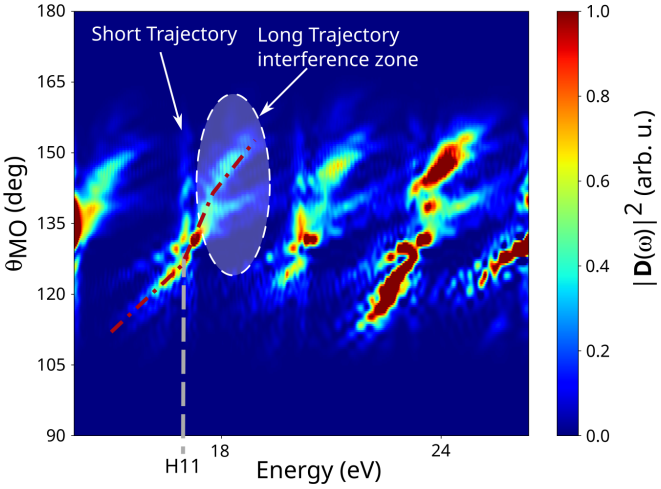

FIG. 10: Same as Fig. 9, zoomed in for energies in the range 16 eV to 25 eV. Special care is paid to H11 indicated by the gray dashed line. The short and long trajectory contributions are indicated. The S shape mentioned in Sec. IV is marked by the red dash-dot line.

shown in Fig. 8 for a peak intensity [1] of 2×10^{14} W/cm^2. In this configuration, the amplitude of the field in the gate region is roughly $E_{in}/2$ for $\theta_{MO} = 45$ deg, where E_{in} is the input field amplitude. The cut-off harmonic is H15 ($24eV$) assuming the cut-off law for linear polarization, and the threshold harmonics (transition from below to above the ionization potential) is H9. The agreement between the theoretical and experimental results is reasonable; in particular, the frequency shift with θ_{MO} appears for all harmonics. One cannot expect more than qualitative agreement from the single atom SFA model. Nevertheless, the essential physical effects are included, and more advanced models including, e.g., propagation effects like in [25], are expected to bring quantitative corrections only. The simulated shift in Fig. 8 is clearly visible in the cut-off region, and even stronger for the plateau harmonics, which is consistent with an emission arising predominantly from the long quantum path for which the α coefficient is large. We note that the particular behavior of the harmonic around 30 eV was also observed in spatially resolved harmonic spectra for linearly polarized fields. It is located in the region of transition from the plateau to the cut-off, which is known to be very sensitive to the intensity of the driving pulse. Therefore, when integrating over the spatial profile of the XUV beam, we expect that this specific behavior will be less pronounced, cf. [34].

To confirm the general validity of our statements and provide more detailed insight, we have performed the same calculations for a higher input intensity of 4×10^{14} W/cm^2 shown in Fig. 9. This intensity is the intensity that would be obtained without the polarization control setup, the actual intensity in the gate is lower. In this configuration, the cut-off harmonic is H21 ($34eV$). Generally speaking, we observe the same trend as for the lower intensity, but the spectral width and shift of the plateau harmonics are larger and allow for further insight. We observe that harmonics belonging to the plateau exhibit more complex structures. Their spectra are composed of several lines corresponding to harmonics emitted at different times that interfere (see also Fig. 10 for a zoomed version in the vicinity of H11). In particular, the short trajectories for which the shifts are rather small can be well identified. They create almost vertical lines in the distribution consistent with small values of α_q. We observe that the same trend is obtained for the experimental results in Fig. 6. In our simulations, the short trajectory peak has an amplitude that changes with θ_{MO}, which is likely due to quantum path interferences [40]. For the long trajectory, the evolution is more complex as it experiences a larger energy shift because the values of α_q are quite large. The spectral sensitivity to peak intensity and envelope shape is thus enhanced compared to the short trajectories or even to the cut-off region.

There is also an important aspect of the dynamics related to the ellipticity property. In Fig. 11, we have plotted the width of the gate – the total width for which the ellipticity is below the critical value of 0.13 – and the position of the gate as a function of θ_{MO}. The position of the polarization gate can be moved in the range ± 10 fs in the vicinity of the centered position for 30 deg $< \theta_{MO} <$ 60 deg. The width of the gate is constant and equals 6 fs. Thus, the gate allows HHG to occur over roughly 2 optical cycles. This means that approximately four half-cycles can effectively contribute to HHG. The

[1] This intensity would be obtained without the polarization control setup, the actual intensity in the experimental gate is lower.

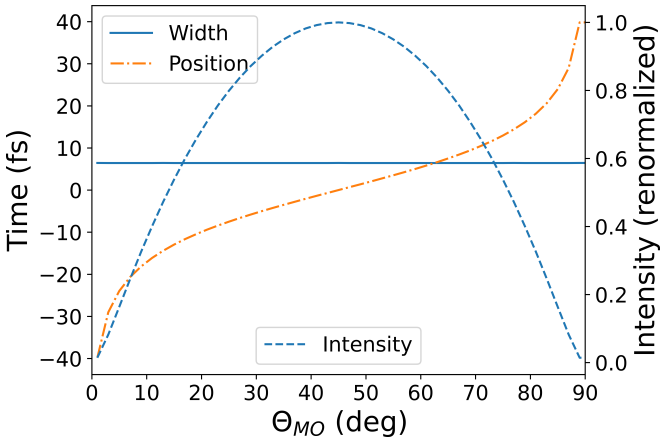

FIG. 11: Position of the center of the polarization gate (orange dot-dashed line) as a function of θ_{MO}. The full blue curve represents the width of the polarization gate vs. θ_{MO}. The relative peak intensity at the center of the polarization gate normalized to its maximum obtained at $\theta_{MO} = 45$ deg is represented by the dashed blue line.

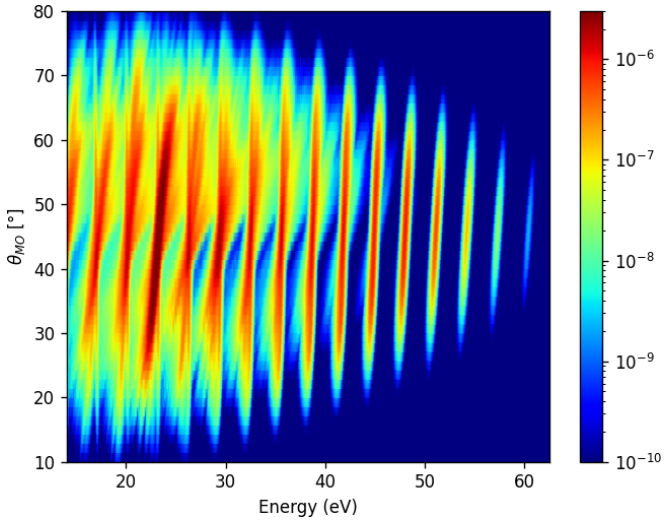

FIG. 12: Same as Fig. 9, but spatially integrated assuming a Gaussian spatial profile for the IR pump field. The plot is in log scale.

complex pattern described by the long trajectory contribution can be explained as follows: The effective frequency exhibits a large energy spread due to the large values of α. Using saddle point analysis, the times t_s that will contribute coherently to a given frequency satisfy the equation $\omega = q\omega_0 + \alpha\frac{\partial I(t)}{\partial t}|_{t=t_s}$. The derivative of the driving field envelope shows that there are several times t_s in the pulse at which a given frequency can be emitted, leading to the complex spatio-spectral ring structure as described in [34]. In [34], the rings appear to be symmetric with respect to the central frequency $q\omega_0$. Under the present conditions, due to the temporal selection imposed by the gate (see Fig. 11), the ring-like structure is cut and only a portion of the ring is observed. This was clearly observed in spatially resolved spectra – results not shown in the article – that allowed for assigning the central part to the short path emission and the outer part of the beam to the long path emission. This simple explanation should be further analyzed since the α parameter is dependent on the pump ellipticity [41].

In order to check if these observations are robust under macroscopic generation conditions, we consider a Gaussian spatial profile for the generating beam and integrate the emitted XUV light over the spatial distribution of intensity. The resulting distribution, which mimics the harmonics emitted from a thin medium considering the macroscopic aspect of the generation, is shown in Fig. 12. The same trends as in Fig. 8 are observed. Most importantly, the harmonic frequencies evolve with θ_{MO} as detailed previously. In the cut-off region, the evolution is regular, and the harmonic frequencies can be tuned over almost one eV, as observed experimentally. In the plateau region, the distribution is more complex and asymmetric around $\theta_{MO} = 45$ deg. As they are well separated for each harmonic in the plateau, we can now clearly assign the contributions of long and short trajectories. The frequency distribution associated with the short trajectories is much less sensitive to θ_{MO} due to the lower α value. On the other hand, the structure related to the long trajectories is much richer, see for instance the region around 25 eV, and the interference zone in Fig. 10. This results from the different instantaneous driver's intensities contributing to different emission times; thus near $\theta_{MO} = 45$ deg each branch resembles the form of a folding-fan due to constructive interferences. This endorses our previous statement at the end of Sect. III.

Despite the overall agreement, there are still discrepancies between experimental and simulation results. The most striking one is the complex structure that appears in the long trajectory contributions that is not observed in the experiment. This is likely due to the fact that the CEP of the driving pulse is not stabilized in the experiments while it is (arbitrarily) fixed to 0 in the simulations (which means that emission times t_s are precisely defined). In the simulations the long trajectory contribution is stronger than the short trajectory while in the experiment the short trajectory has a similar or stronger signal. This may arise from the fact that the input slit of the spectrometer favors the low diverging short path harmonic over the highly diverging long path emission, an effect that is not included in the simulations. This might artificially boost the signal arising from the short path emission in the experiment.

An interesting feature is that in Fig. 12 for a given harmonic an S-shaped structure with θ_{MO} appears (see also Fig. 10 for more details). This structure is particularly visible for the harmonic H17, and can be explained by the fact that the position of the gate behaves like an S-shaped as a function of θ_{MO}, cf. Fig. 11. It becomes

less visible for higher order harmonics which are emitted solely at the maximum of the field amplitude. In other words, the harmonic spectrum plotted versus θ_{MO} is very sensitive to the position of the polarization gate as a function of θ_{MO}. As such, it can be used as a diagnostic tool to get further insight into the properties of the polarization gate. More quantitatively, for harmonics in the cut-off region, we can approximate $\alpha_{\text{cut-off}} \approx 13$. In the deep plateau region, for the first harmonic in the plateau, we have $\alpha_{\text{short}} \approx 1-5$ and $\alpha_{\text{long}} \approx 20-26$ [41]. Thus, the expression of the frequency Eq. (2) implies a different energy shift for long and short trajectory contributions, as can be observed in Figs. 6 and 12. Having identified the short trajectories as the less tilted ones, the evolution of the slope of the shift agrees with an increase of α_{short} with harmonic order. From Fig. 7 we can estimate the energy shift for the short trajectory of H11 to 250 meV and to 1.1 eV for the long path. For the harmonic H19, which lies in the cut-off region, the observed shift is 600 meV, in agreement with the previous sentence. For H11, we can extract the ratio between the energy shifts as $\Delta E_{\text{long}}/\Delta E_{\text{short}} \approx 4.4$ from our experimental results. According to our interpretation, it should correspond to the ratio of the parameters α_q for long and short trajectories of H11. The values $\alpha_{\text{short}} = 5.4$ and $\alpha_{\text{long}} = 26$ are theoretically obtained for H11 by saddle point analysis [36], and the ratio $\alpha_{\text{long}}/\alpha_{\text{short}} \approx 4.8$ is in good agreement with the experimental findings.

The spectral width of the harmonics is an indirect signature of the width of the polarization gate and temporal confinement. The theory predicts that the gate width is constant with respect to θ_{MO} for each harmonic regardless of the position of the gate, cf. Fig. 11, and shrinks as the harmonic order increases. The spectral FWHM vs. θ_{MO} extracted from Fig. 7 for each harmonic is summarized in table I in App. B. It shows that the spectral width of each harmonic varies within 10% for plateau harmonics and within 20% for cut-off harmonics. These experimental values are compatible with a constant gate width. Furthermore, we calculated a mean spectral width of each harmonic and extracted the minimum compatible gate duration from this FWHM using the uncertainty relation with a Gaussian profile. The gate width obtainable with our polarization control setup and known pulse characteristics can also be calculated from SFA [41, 42] and is represented in table II in App. B. Both values agree within 20%.

There is a last feature that is not reproduced in the SFA simulations and that is also in agreement with a controlled gate displacement. It appears at a photon energy just below 16 eV in Figs. 5 and 6 (underlined by the dahed lines), and only at angles where the polarization gate is in the falling front of the pulse. This feature can be attributed to the emission from Rydberg states [43] that is not included in the SFA model. The fact that the Rydberg contribution mainly occurs in the falling front is interpreted as follows: We only observe XUV emission from Rydberg states with L=±1. If the Rydberg states are populated during the rising edge of the pulse (i.e. as the amplitude of the field increases), the excitation is destroyed by ionization later in the pulse for higher field amplitude or by coupling with other Rydberg states. In contrast, if excitation of these Rydberg states occurs in the falling edge of the pulse, they remain populated since the amplitude of the field decreases at later times. They can then emit light afterwards.

V. CONCLUSION

We have studied in detail the characteristics of the polarization gating by changing the amplitude ratio of the two delayed counter-rotating pulses controlled by two birefringent plates composed of a thick plate and a zero-order quarter waveplate. This setup allows for asymmetric polarization gating (APG). We have shown that it can be used as a controllable polarization gate, in particular, it is possible to control the position of the gate inside the pulse intensity profile without changing the gate width and thereby the XUV temporal confinement. We found that the experimental spectra agree well with a gate displacement without gate distortion, keeping the same temporal confinement. The experimental findings are also in good agreement with our SFA modeling results, which, however, do not describe all the features; in particular, the contribution of Rydberg states is not included. Furthermore, we have demonstrated the ability of APG to control the central frequency of the harmonic comb. This frequency control is related to the phase of the emitting dipole and is thus different for short and long trajectories. This property of HHG in asymmetric polarization gating can be of interest to the use of HHG as an XUV source in spectroscopy where fine control of the frequency is a requirement. Compared to using an optical parametric amplifier to tune the driving wavelength, the present approach requires considerably less experimental efforts, and provides additional degrees of freedom as it can be interesting to independently tune the harmonic originating from the short and long trajectories. The gate can be precisely located without deformation inside the falling or rising part of the pulse. We report that under our experimental conditions, the efficiency of HHG is maximum when the gate is located in the falling front, which can also be of interest to optimize confined XUV emission.

VI. ACKNOWLEDGEMENTS

Computer time for this study was provided by the computing facilities of the MCIA (Mésocentre de Calcul Intensif Aquitain). We acknowledge stimulating discussions with E. Mével, V. Loriot, F. Lépine and Ch. Bordas. J. V. acknowledges the support by the project Advanced research using high intensity laser produced photons and particles (CZ.02.1.01/0.0/0.0/16_019/0000789)

from European Regional Development Fund (ADONIS).

Appendix A: Theoretical description of fields

Assuming a Gaussian envelope of the input field, the rotation ($\mathbb{R}_\theta$) and delay ($\mathbb{D}_\delta$) matrices are provided by

$$\mathbb{R}_\theta = \begin{pmatrix} \cos(\theta_{MO}) & \sin(\theta_{MO}) \\ -\sin(\theta_{MO}) & \cos(\theta_{MO}) \end{pmatrix}, \tag{A1}$$

$$\mathbb{D}_\delta = \begin{pmatrix} 1 & 0 \\ 0 & ie^{i\omega\delta}e^{\beta.(2.t.\delta-\delta^2)} \end{pmatrix}, \tag{A2}$$

where $\beta = 2\ln(2)/\tau^2$. δ is the delay introduced by the plate, while τ is the parameter used to describe the Gaussian envelope (proportional to its FWHM). The two dimensions of the matrices correspond to the two canonical axes (fast and slow axis) on which the polarization state of the light is projected. Using these two matrices, the action of each plate on the field can be written as

$$\mathbb{O}_{MO} = \mathbb{R}_{\theta_{MO}}\mathbb{D}_\delta\mathbb{R}^{-1}_{\theta_{MO}}, \tag{A3}$$

$$\mathbb{O}_{ZO} = \mathbb{R}_{\theta_{MO}-\frac{\pi}{4}}\mathbb{D}_0\mathbb{R}^{-1}_{\theta_{MO}-\frac{\pi}{4}}, \tag{A4}$$

where the matrices $\mathbb{O}_M^{\theta_{MO}}$ and $\mathbb{O}_0^{\theta_{MO}}$ represent the multi-order waveplate and the 0^{th} order waveplate action, respectively. The input field is set to $\mathbf{E}_{\text{in}} = (E(t), 0)$ and the resulting field is $\mathbf{E}_{\text{out}} = \mathbb{O}_{ZO}\mathbb{O}_{MO}\mathbf{E}_{\text{in}}$. The resulting field is of the form of Eq. (7), with a complex-valued amplitude and a relative phase that depend on θ_{MO}. It is thus the sum of two counter-rotating fields.

In order to match the experimental conditions, we have to make the transformation $\theta_{MO} \to \theta_{MO} + \frac{\pi}{2}$. This is due to the freedom of having either the fast or slow axis as a reference.

Appendix B: Experimental data

[1] S. Hädrich, M. Krebs, A. Hoffmann, A. Klenke, J. Rothhardt, J. Limpert, and A. Tünnermann. *Light: Science and Applications*, 4:e320, 2015.

[2] S. Fuchs, C. Rödel, A. Blinne, U. Zastrau, M. Wünsche, V. Hilbert, L. Glaser, J. Viefhaus, E. Frumker, P. B. Corkum, E. Förster, and G. G. Paulus. *Scientific Reports*, 6:20658, 2016.

[3] L. Quintard, V. Strelkov, J. Vabek, O. Hort, A. Dubrouil, D. Descamps, F. Burgy, C. Péjot, E. Mével, F. Catoire, and E. Constant. *Sci. Adv.*, 5:eaau7175, 2019.

[4] B. Vodungbo, A. B. Sardinha, J. Gautie, G. Lambert, C. Valentin, M. Lozano, G. Iaquaniello, F. Delmotte, S. Sebban, J. Lüning, and Ph. Zeitoun. *Opt. Exp.*, 19:4346, 2011.

[5] T. Gaumnitz, A. Jain, Y. Pertot, M. Huppert, I. Jordan, F. Ardana-Lamas, and H. J. Wörner. *Opt. Express*, 25:27506–27518, 2017.

[6] J. Li, X. Ren, Y. Yin, K. Zhao, A. Chew, Y. Cheng, E. Cunningham, Y. Wang, S. Hu, Y. Wu, M. Chini, and Z. Chang. *Nat. Com.*, 8:186, 2017.

[7] P. Agostini and L.F. DiMauro. *Rep. Prog. Phys.*, 67:813, 2004.

[8] F. Krausz and M. Ivanov. *Rev. Mod. Phys.*, 81:163, 2009.

[9] Z. Chang and P. B. Corkum. *J. Opt. Soc. Am. B*, 27:B9–B17, 2010.

[10] F. Calegari, G. Sansone, S. Stagira, C. Vozzi, and M. Nisoli. *J. Phys. B*, 49:062001, 2016.

[11] J.P. Marangos. *J. Phys. B*, 49:132001, 2016.

[12] A. L. Cavalieri, N. Müller, Th. Uphues, V. S. Yakovlev, A. Baltuška, B. Horvath, B. Schmidt, L. Blümel, R. Holzwarth, S. Hendel, M. Drescher, U. Kleineberg, P. M. Echenique, R. Kienberger, F. Krausz, and U. Heinzmann. *Nature*, 449:1029–1032, 2007.

[13] T. Heinrich, M. Taucer, O. Kfir, P. B. Corkum, A. Staudte, C. Ropers, and M. Sivis. *Nature Communications*, 12:3723, 2021.

[14] R. Geneaux, H. J. B. Marroux, A. Guggenmos, D. M. Neumark, and S. R. Leone. *Phil. Trans. R. Soc. A*, 377:0463, 2019.

[15] K. Kaneshima, Y. Ninota, and T. Sekikawa. *Optics Express*, 26:31039–31054, 2018.

[16] P. B. Corkum, N. H. Burnett, and M. Y. Ivanov. *Opt. Lett.*, 19:1870–1872, 1994.

[17] C. Altucci, C. Delfin, L. Roos, M. B. Gaarde, A. L'Huillier, I. Mercer, T. Starczewski, and C.-G. Wahlström. *Phys. Rev. A*, 58:3934, 1998.

[18] V. T. Platonenko and V. V. Strelkov. *J. Opt. Soc. Am. B*, 16:435–440, 1999.

[19] O. Tcherbakoff, E. Mével, D. Descamps, J. Plumridge, and E. Constant. *Phys. Rev. A*, 68:043804, 2003.

[20] Y. Mairesse, O. Gobert, P. Breger, H. Merdji, P. Meynadier, P. Monchicourt, M. Perdrix, P. Salières, and B. Carré. *Phys. Rev. Lett.*, 94:173903, 2005.

[21] Zenghu Chang. *Phys. Rev. A*, 76:051403, 2007.

[22] I. J. Sola, E. Mével, L. Elouga, E. Constant, V. Strelkov, L. Poletto, P. Villoresi, E. Benedetti, J.-P. Caumes, S. Stagira, C. Vozzi, G. Sansone, and M. Nisoli. *Nat. Phys.*, 2:319–322, 2006.

[23] G. Sansone, E. Benedetti, F. Calegari, C. Vozzi, L. Avaldi, R. Flammini, L. Poletto, P. Villoresi, C. Altucci, R. Velotta, S. Stagira, S. De Silvestri, and M. Nisoli. *Science*, 314:443, 2006.

[24] P. Tzallas, E. Skantzakis, C. Kalpouzos, E. P. Benis, G. D. Tsakiris, and D. Charalambidis. *nat. Phys.*, 3:846–850, 2007.

[25] Gao Chen, Eric Cunningham, and Zenghu Chang. *Journal of Modern Optics*, 64(10-11):952, 2017.

[26] K. S. Budil, P. Salières, Anne L'Huillier, T. Ditmire, and M. D. Perry. *Phys. Rev. A*, 48:R3437–R3440, 1993.

[27] Philippe Antoine, Anne L'Huillier, Maciej Lewenstein, Pascal Salières, and Bertrand Carré. *Phys. Rev. A*, 53:1725–1745, 1996.

θ_{MO}	H11	H13	H15	H17	H19
113 deg	400 (± 20)	410 (± 20)	380 (± 30)	n.d.	n.d
117 deg	410 (± 20)	380 (± 20)	380 (± 30)	480 (± 40)	n.d
121 deg	420 (± 20)	410 (± 20)	390 (± 30)	470 (± 40)	560 (± 40)
125 deg	450 (± 20)	400 (± 20)	400 (± 30)	560 (± 20)	550 (± 30)
129 deg	380 (± 20)	420 (± 20)	420 (± 30)	490 (± 20)	520 (± 30)
131 deg	350 (± 20)	430 (± 20)	400 (± 30)	480 (± 20)	520 (± 30)
135 deg	420 (± 20)	420 (± 20)	430 (± 30)	490 (± 20)	540 (± 30)
139 deg	400 (± 20)	400 (± 20)	450 (± 30)	540 (± 20)	580 (± 30)
141 deg	370 (± 20)	380 (± 20)	540 (± 30)	570 (± 20)	n.d
145 deg	380 (± 20)	420 (± 20)	580 (± 30)	n.d.	n.d
$< FWHM >$	398 (± 20)	407 (± 20)	437 (± 30)	510 (± 40)	545 (± 40)

TABLE I: Table showing the measured harmonic spectral width as a function of θ_{MO} for H11 to H19. The last line is the mean FWHM for each harmonic. All energies are expressed in meV.

	H11	H13	H15	H17	H19
τ_{gate} (fs) (gaussian)	4.6 (±0.3 fs)	4.5 (±0.3 fs)	4.1 (±0.3 fs)	3.6 (±0.2 fs)	3.4 (±0.2 fs)
τ_{gate} (fs) (SFA)	6.1 (±0.2 fs)	5.4 (±0.2 fs)	4.7 (±0.2 fs)	4.6 (±0.2 fs)	4.2 (±0.2 fs)

TABLE II: Table showing the width of the polarization gate (fs) for H11 to H19 estimated with the harmonic spectral width and the uncertainty principle. This estimate relies on the fact that the harmonic spectral width is only due to temporal confinement and is therefore an underestimation of the real gate width. The second line is the result obtained using the SFA model.

[28] N. Tancogne-Dejean, O. D. Mücke, F. X. Kärtner, and A. Rubio. *Nat. Com.*, 8:745, 2017.

[29] Y. S. You, D.A. Reis, and S. Ghimire. *Nat. Phys.*, 13:345–349, 2017.

[30] E. Cunningham and Z. Chang. *IEEE Journal of Selected Topics in Quantum Electronics*, 21:2426655, 2015.

[31] P. Lan, P. Lu, F. Li, Q. Li, W. Hong, Q. Zhang, Z. Yang, and X. Wang. *Optics Express*, 16:17542–17553, 2008.

[32] H. Mashiko, S. Gilbertson, C. Li, S. D. Khan, M. M. Shakya, E. Moon, and Z. Chang. *Phys. Rev. Lett.*, 100:103906, 2008.

[33] A. V. Andrianov and E.A. Anashkina. *Results in Physics*, 29:104740, 2021.

[34] F. Catoire, A. Ferré, O. Hort, A. Dubrouil, L. Quintard, D. Descamps, S. Petit, F. Burgy, E. Mével, Y. Mairesse, and E. Constant. *Phys. Rev. A*, 94:063401, 2016.

[35] M. B. Gaarde, F. Salin, E. Constant, Ph. Balcou, K. J. Schafer, K. C. Kulander, and A. L'Huillier. *Phys. Rev. A*, 59:1367–1373, 1999.

[36] M. Lewenstein, Ph. Balcou, M. Yu. Ivanov, A. L'Huillier, and P. B. Corkum. *Phys. Rev. A*, 49:2117–2132, 1994.

[37] A. Nayak, M. Dumergue, S. Kühn, S. Mondal, T. Csizmadia, N.G. Harshitha, M. Füle, M. U. Kahaly, B. Farkas, B. Major, V. Szaszkó-Bogár, P. Földi, S. Majorosi, N. Tsatrafyllis, E. Skantzakis, L. Neoričić, M. Shirozhan, G. Vampa, K. Varjú, P. Tzallas, G. Sansone, D. Charalambidis, and S. Kahaly. *Physics Reports*, 833:1–52, 2019.

[38] A.-T. Le, H. Wei, C. Jin, and C.D. Lin. *J. Phys. B*, 49:053001, 2016.

[39] E. Mansten, J. M. Dahlström, J. Mauritsson, T. Ruchon, A. L'Huillier, J. Tate, M. B. Gaarde, P. Eckle, A. Guandalini, M. Holler, F. Schapper, L. Gallmann, and U. Keller. *Phys. Rev. Lett.*, 102:083002, 2009.

[40] A. Zaïr, M. Holler, A. Guandalini, F. Schapper, J. Biegert, L. Gallmann, U. Keller, A.S. Wyatt, A. Monmayrant, I.A. Walmsley, E. Cormier, T. Auguste, J.P. Caumes, and P. Salières. *Phys. Rev. Lett.*, 100:143902, 2008.

[41] V. Strelkov, A. Zaïr, O. Tcherbakoff1, R. López-Martens, E. Cormier, E. Mével, and E. Constant. *Laser Physics*, 15:1, 2005.

[42] V. Strelkov, A. Zaïr, O. Tcherbakoff1, R. López-Martens, E. Cormier, E. Mével, and E. Constant. *J. Phys. B*, 38:L161, 2005.

[43] S. Beaulieu, S. Camp, D. Descamps, A. Comby, V. Wanie, S. Petit, F. Légaré, K. J. Schafer, M. B. Gaarde, F. Catoire, and Y. Mairesse. *Phys. Rev. Lett.*, 117:203001, 2016.